
A MULTI-MODAL FUSION FRAMEWORK FOR BRAIN TUMOR SEGMENTATION BASED ON 3D SPATIAL-LANGUAGE-VISION INTEGRATION AND BIDIRECTIONAL INTERACTIVE ATTENTION MECHANISM *

Ming-Da Zhang¹, Kai-Wen Pan¹

¹School of Software, Yunnan University
No. 2 North Cuihu Road, Kunming, 650091
Yunnan Province, China
mingda.zhang@email.com

ABSTRACT

Purpose: This study aims to develop a novel multi-modal fusion framework for brain tumor segmentation that integrates spatial-language-vision information through bidirectional interactive attention mechanisms to improve segmentation accuracy and boundary delineation. **Methods:** We propose two core components: Multi-modal Semantic Fusion Adapter (MSFA) integrating 3D MRI data with clinical text descriptions through hierarchical semantic decoupling, and Bidirectional Interactive Visual-semantic Attention (BIVA) enabling iterative information exchange between modalities. The framework was evaluated on BraTS 2020 dataset comprising 369 multi-institutional MRI scans. **Results:** The proposed method achieved average Dice coefficient of 0.8505 and 95% Hausdorff distance of 2.8256mm across enhancing tumor, tumor core, and whole tumor regions, outperforming state-of-the-art methods including SCAU-Net, CA-Net, and 3D U-Net. Ablation studies confirmed critical contributions of semantic and spatial modules to boundary precision. **Conclusion:** Multi-modal semantic fusion combined with bidirectional interactive attention significantly enhances brain tumor segmentation performance, establishing new paradigms for integrating clinical knowledge into medical image analysis.

Keywords Multi-modal MRI fusion · Brain tumor segmentation · Vision-language integration · Bidirectional interactive attention · Semantic-spatial constraints · 3D medical image analysis

1 Introduction

Multi-modal magnetic resonance imaging brain tumor segmentation represents a fundamental challenge in computational neuro-oncology, requiring precise delineation of tumor sub-regions with distinct biological and radiological characteristics [1, 2]. This complexity arises from heterogeneous tumor manifestations across MRI sequences, subtle tissue boundaries, and complex spatial associations among hierarchical tumor sub-regions [3]. Contemporary approaches predominantly employ visual feature extraction from multi-sequence MRI data, treating segmentation as image-based pattern recognition while neglecting semantic information from clinical practice [4, 5].

Current methodologies face three principal limitations. First, existing methods inadequately model hierarchical spatial relationships in brain tumor pathology, particularly the nested structure of enhancing tumor (ET) \subseteq tumor core (TC) \subseteq whole tumor (WT) [6]. Second, semantic knowledge in clinical descriptions, pathological classifications, and diagnostic terminology remains largely untapped [7, 8]. Third, traditional multi-modal methods employ static fusion strategies lacking adaptability for inter-patient variability and complex tumor presentations [9].

**Citation:* Zhang, M.-D., Pan, K.-W. A Multi-Modal Fusion Framework for Brain Tumor Segmentation Based on 3D Spatial-Language-Vision Integration and Bidirectional Interactive Attention Mechanism. arXiv:XXXX.XXXXX

This study addresses these limitations through two principal methodologies:

1. **Multi-modal Semantic Fusion Adapter (MSFA)**: Integrates 3D medical imaging with NLP through hierarchical semantic decoupling, coordinating fusion of spatial constraints and visual-semantic features.
2. **Bidirectional Interactive Visual-semantic Attention (BIVA)**: Employs spatially-preserving progressive interaction for dynamic feature refinement via iterative multi-round processes.

2 Related Work

2.1 Vision-Language Models in Medical Imaging Applications

Brain tumor segmentation has evolved from traditional approaches to deep learning methods. The BraTS challenges established standardized protocols defining three regions: whole tumor (WT), tumor core (TC), and enhancing tumor (ET) [1]. Current approaches include architectural improvements (nnU-Net [6]), Transformer-based methods [4, 5], and multi-task frameworks [10]. However, existing methods inadequately handle tumor heterogeneity and underutilize clinical semantic information [3].

This study presents an end-to-end architecture integrating spatial-language-visual information through: multi-sequence MRI inputs with clinical descriptions, specialized adapters coordinating spatial constraints with visual-semantic features, dynamic iterative exchange mechanisms, and 3D segmentation decoder output.

2.2 Multi-modal Fusion

Multi-modal medical image analysis has progressed from simple concatenation to sophisticated integration methods. Early approaches using averaging failed to capture inter-modal relationships [11]. Recent methods employ cross-modal attention and adversarial training [12], yet predominantly focus on visual modalities.

The proposed MSFA integrates visual features, semantic constraints, and spatial relationships through modality preservation, semantic alignment, and adaptive weighting, overcoming static fusion limitations.

2.3 Bidirectional Interaction Mechanisms

Traditional attention mechanisms employ unidirectional information flow, limiting mutual enhancement between modalities [13]. Current methods treat semantic information as static guidance without dynamic exchange [14, 15]. Interactive mechanisms remain limited to simple connections without quality assessment [16].

The proposed BIVA implements iterative information exchange through semantic-to-visual and visual-to-semantic paths, with multi-dimensional quality assessment and intelligent convergence control.

3 Methods

The proposed framework adopts hierarchical architecture design, achieving precise tumor segmentation through collaborative operation of MSFA and BIVA. As shown in Figure 1, the framework accepts multi-sequence MRI images and clinical descriptions, performs multi-modal feature extraction through MSFA, achieves dynamic interaction optimization through BIVA, and outputs segmentation results through 3D decoder.

3.1 Multi-modal Semantic Fusion Adapter Architecture

As shown in Figure 2, MSFA achieves specialized processing and unified fusion through three parallel branches: visual processing for multi-sequence 3D MRI data, semantic processing for clinical text descriptions, and spatial constraint encoding for anatomical prior knowledge.

MSFA constitutes the foundational component designed to coordinate seamless integration of spatial, language, and visual information modalities. The architectural design follows modality preservation, semantic alignment, and adaptive weighting principles [17].

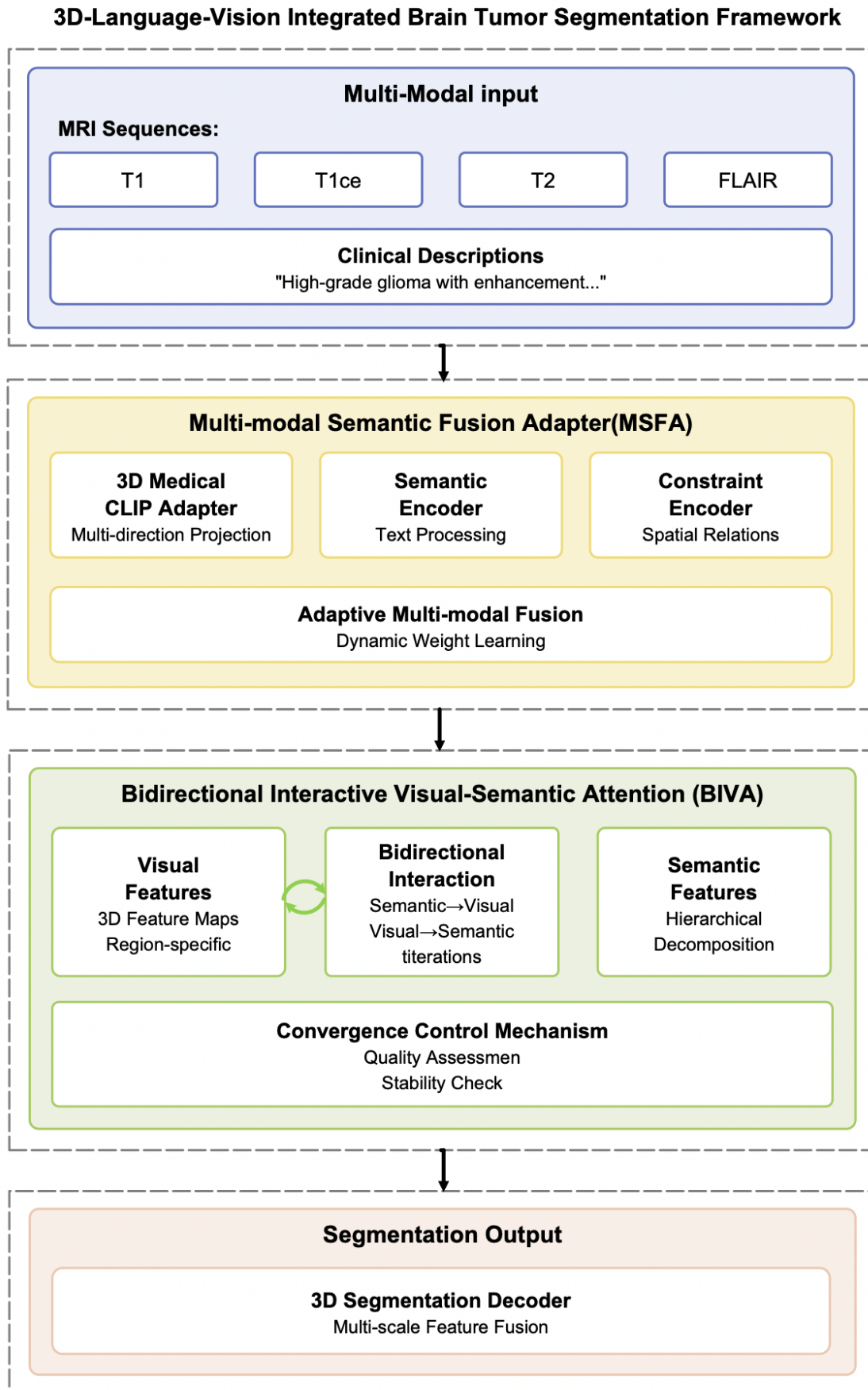


Figure 1: Overall framework architecture. The proposed multi-modal fusion framework integrates MRI sequences with clinical text descriptions through MSFA and BIVA components for brain tumor segmentation

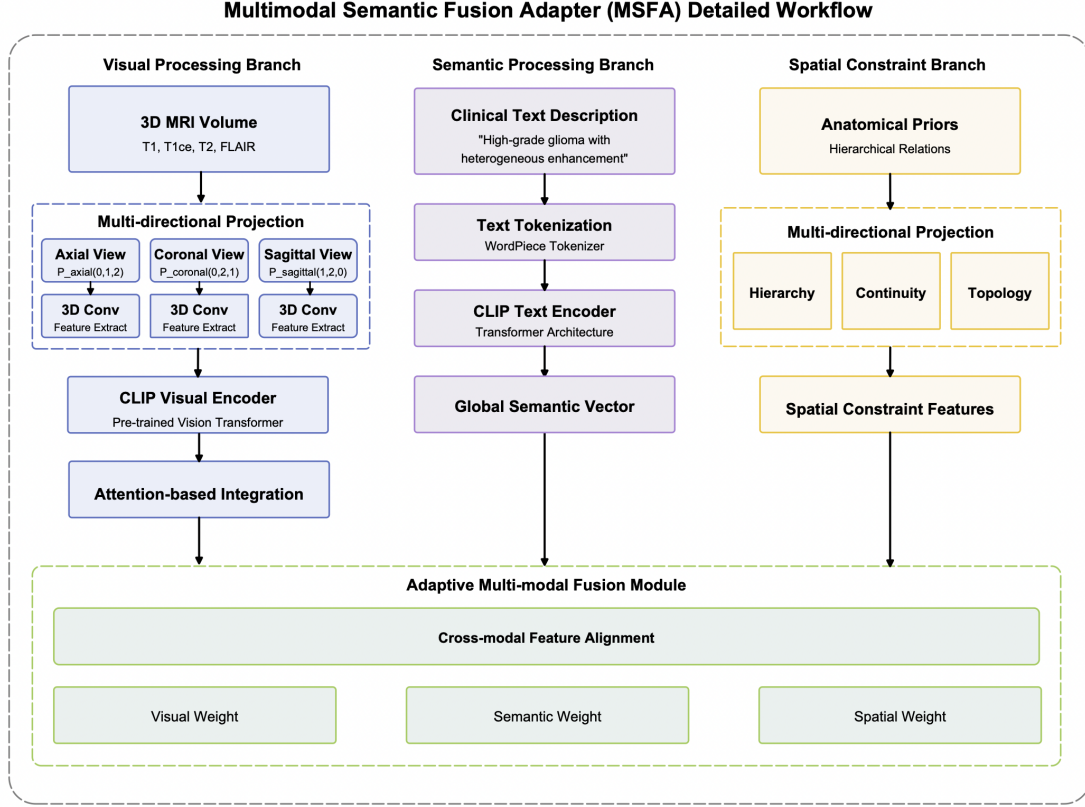


Figure 2: Multi-modal Semantic Fusion Adapter (MSFA) architecture. Three parallel branches process visual, semantic, and spatial constraint information with adaptive fusion module for unified feature representation

3.1.1 Visual Processing Branch

The visual processing branch processes multi-sequence 3D MRI data through multi-directional projection along axial, coronal, and sagittal planes. Features undergo dynamic fusion through attention-based integration:

$$\mathbf{F}_{visual} = \sum_i \alpha_i \mathbf{F}_{visual}^{(i)}, \quad \text{where} \quad \alpha_i = \text{softmax}(\mathbf{W}_a^T \tanh(\mathbf{W}_b \mathbf{F}_{visual}^{(i)})) \quad (1)$$

In the dynamic fusion mechanism of visual processing branch, \mathbf{F}_{visual} represents the final fused visual feature vector, $\mathbf{F}_{visual}^{(i)}$ denotes direction-specific feature vector from the i -th projection direction (axial, coronal, sagittal), α_i represents dynamic weight coefficient normalized through softmax function for balancing importance of features from different directions. \mathbf{W}_a and \mathbf{W}_b are two learnable attention parameter matrices implementing nonlinear assessment of feature importance through two-layer neural network structure, where tanh activation function introduces nonlinear transformation, enabling the model to adaptively select most diagnostically valuable view information based on current tumor morphological characteristics.

3.1.2 Semantic Processing Branch

The semantic processing branch converts clinical text descriptions into computable semantic representations through WordPiece tokenization and Transformer-based CLIP text encoder, generating global semantic vectors capturing diagnostic information and pathological features.

3.1.3 Spatial Constraint Branch

The spatial constraint branch models three core constraints through neural network encoder:

Hierarchical relationship constraint models nested structure of $ET \subseteq TC \subseteq WT$:

$$\mathcal{L}_{hierarchy} = \sum_{v \in \mathcal{V}} \max(0, P_{ET}(v) - P_{TC}(v)) + \max(0, P_{TC}(v) - P_{WT}(v)) \quad (2)$$

In the hierarchical relationship constraint loss function, $\mathcal{L}_{hierarchy}$ represents overall hierarchical constraint loss value, \mathcal{V} denotes the set of all voxel positions in 3D medical image, v represents individual voxel position index. $P_{ET}(v)$, $P_{TC}(v)$, $P_{WT}(v)$ respectively represent model-predicted probabilities of enhancing tumor, tumor core, and whole tumor at voxel position v , these probability values typically normalized between 0 and 1 through softmax function. The max function ensures penalty loss only occurs when hierarchical relationships are violated (i.e., sub-region probability greater than parent region probability), thereby maintaining medical prior nested structure where enhancing tumor is contained within tumor core, and tumor core is contained within whole tumor.

Continuity constraint ensures spatial continuity of adjacent voxels:

$$\mathcal{L}_{continuity} = \sum_{v \in \mathcal{V}} \sum_{u \in \mathcal{N}(v)} \|\mathbf{f}_{spatial}(v) - \mathbf{f}_{spatial}(u)\|_2^2 \quad (3)$$

In the continuity constraint loss function, $\mathcal{L}_{continuity}$ represents overall spatial continuity loss value, \mathcal{V} still denotes the set of all voxel positions, v and u respectively represent central voxel and its neighboring voxel position indices. $\mathcal{N}(v)$ represents spatial neighborhood set of voxel v , typically adopting 6-connected or 26-connected 3D neighborhood definition. $\mathbf{f}_{spatial}(v)$ and $\mathbf{f}_{spatial}(u)$ respectively represent spatial feature representation vectors at voxel positions v and u , $\|\cdot\|_2^2$ denotes squared Euclidean distance, this constraint ensures spatial smoothness and continuity of segmentation results by minimizing differences in feature representations between adjacent voxels.

Topology constraint maintains morphological properties of tumor regions:

$$\mathcal{L}_{topology} = \lambda_{shape} \cdot \text{Dice}(\mathbf{M}_{pred}, \mathbf{M}_{topology}) + \lambda_{boundary} \cdot \|\nabla \mathbf{M}_{pred}\|_1 \quad (4)$$

In the topology constraint loss function, $\mathcal{L}_{topology}$ represents loss value for maintaining morphological properties of tumor regions, λ_{shape} and $\lambda_{boundary}$ are two weight coefficients balancing importance of different topology constraints. \mathbf{M}_{pred} represents model-predicted segmentation mask, $\mathbf{M}_{topology}$ represents topology reference mask constructed based on anatomical prior knowledge. Dice function calculates similarity between predicted mask and topology reference mask, ∇ represents gradient operator, $\|\nabla \mathbf{M}_{pred}\|_1$ calculates L1 norm of predicted mask gradient to assess boundary smoothness, this constraint ensures segmentation results maintain reasonable shape features while having smooth boundary contours.

3.1.4 Adaptive Multi-modal Fusion Module

The adaptive multi-modal fusion module intelligently integrates outputs from three branches through dynamic weight learning:

$$\begin{aligned} \mathbf{w} &= \text{softmax}(\mathbf{W}_{gate}^T \sigma(\mathbf{W}_{fusion} [\tilde{\mathbf{F}}_{visual}; \tilde{\mathbf{S}}_{semantic}; \tilde{\mathbf{F}}_{spatial}] + \mathbf{b}_{fusion})) \\ &= [w_{visual}, w_{semantic}, w_{spatial}]^T \end{aligned} \quad (5)$$

In the dynamic weight learning mechanism of adaptive multi-modal fusion module, \mathbf{w} represents the vector containing three modal weights, decomposed into visual weight w_{visual} , semantic weight $w_{semantic}$, and spatial constraint weight $w_{spatial}$. \mathbf{W}_{gate} is the weight parameter matrix of gating mechanism, \mathbf{W}_{fusion} is the transformation matrix for feature fusion, \mathbf{b}_{fusion} is the bias vector. $\tilde{\mathbf{F}}_{visual}$, $\tilde{\mathbf{S}}_{semantic}$, $\tilde{\mathbf{F}}_{spatial}$ respectively represent aligned visual features, semantic features, and spatial constraint features, brackets denote feature concatenation operation, σ represents sigmoid activation function. This mechanism ensures the sum of three modal weights equals 1 through softmax function, implementing dynamic fusion strategy that adaptively adjusts relative importance of each modality based on current input features.

3.2 Bidirectional Interactive Visual-semantic Attention Mechanism

As shown in Figure 3, BIVA achieves dynamic optimization through iterative bidirectional information exchange between visual and semantic features until convergence.

BIVA establishes dynamic iterative information exchange systems based on mutual refinement between visual and semantic modalities [18].

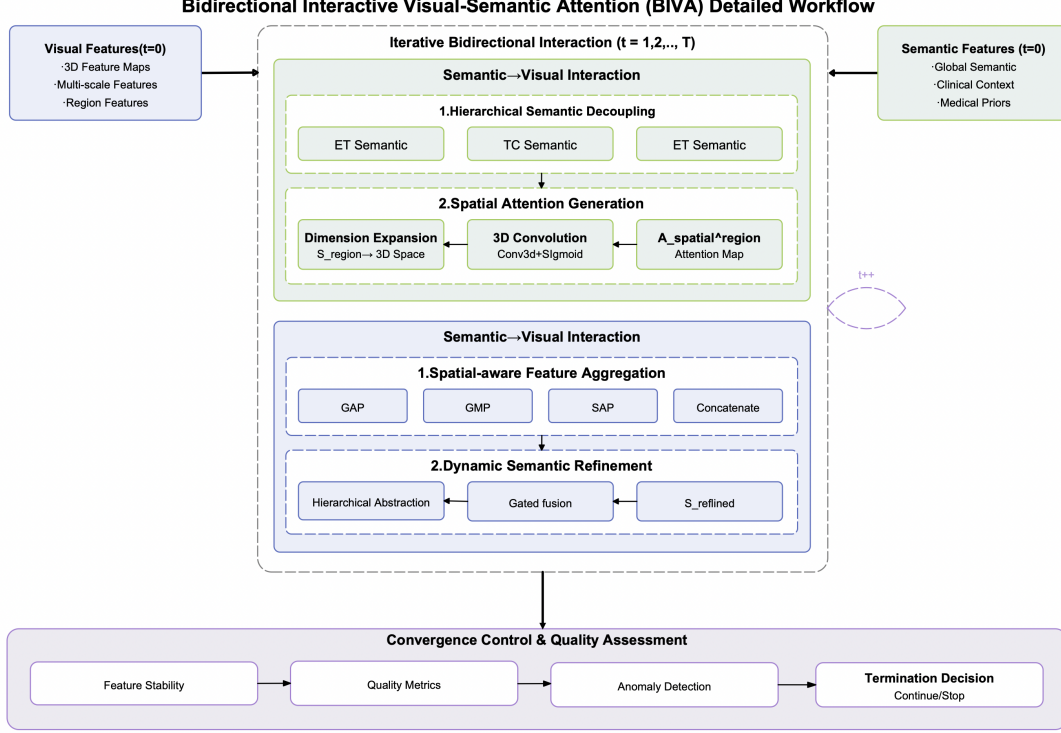


Figure 3: Bidirectional Interactive Visual-semantic Attention (BIVA) mechanism. Iterative information exchange between visual and semantic modalities with quality assessment and convergence control

3.2.1 Semantic-to-Visual Interaction Implementation

The semantic-to-visual interaction addresses how abstract semantic knowledge guides visual feature learning through hierarchical semantic decoupling and spatial attention generation. Region-specific semantic vectors generate 3D spatial attention maps:

$$\mathbf{A}_{spatial}^{region} = \sigma(\text{Conv3D}(\text{Expand}(\mathbf{S}_{region} \odot \mathbf{W}_{region}))) \quad (6)$$

In the spatial attention generation mechanism, $\mathbf{A}_{spatial}^{region}$ represents 3D spatial attention map generated for specific anatomical region, \mathbf{S}_{region} denotes region-specific semantic vector obtained through hierarchical semantic decoupling. \mathbf{W}_{region} is weight parameter matrix specifically learned for that region, \odot represents element-wise multiplication operation for point-wise fusion of semantic information with regional weights. Expand function expands low-dimensional semantic vector to spatial dimensions matching 3D medical image, Conv3D represents 3D convolution operation, σ is sigmoid activation function ensuring final attention weight values are controlled within reasonable range of 0 to 1, thereby achieving precise spatial guidance of semantic information on 3D visual features.

3.2.2 Visual-to-Semantic Interaction Framework

The visual-to-semantic interaction extracts high-level semantic concepts through spatially-aware feature aggregation and dynamic semantic refinement. Feature aggregation combines multiple pooling strategies [19]:

$$\mathbf{F}_{aggregated} = \text{Concat}[\text{GAP}(\mathbf{F}), \text{GMP}(\mathbf{F}), \text{SAP}(\mathbf{F})] \quad (7)$$

In the spatially-aware feature aggregation process, $\mathbf{F}_{aggregated}$ represents compact feature vector aggregated through multiple pooling strategies, \mathbf{F} denotes input high-dimensional 3D feature tensor. GAP, GMP, SAP respectively represent global average pooling, global max pooling, and spatial adaptive pooling operations, where GAP captures overall feature statistical properties by computing average values across all spatial positions, GMP identifies most salient feature activations by extracting maximum response values, SAP maintains important spatial structure information through adaptive sampling. Concat represents tensor concatenation operation, concatenating three pooling results along

feature dimension, forming comprehensive feature representation that fuses global statistical information, salient feature responses, and spatial structure information.

Hierarchical abstraction converts visual features to semantic representations:

$$\mathbf{S}_{visual} = \mathcal{H}_{abstract}(\mathbf{F}_{aggregated} + \mathcal{R}_{residual}(\mathbf{F}_{aggregated})) \quad (8)$$

In the hierarchical abstraction conversion process, \mathbf{S}_{visual} represents semantic representation vector extracted from visual features, $\mathcal{H}_{abstract}$ denotes hierarchical abstraction network function responsible for mapping low-level visual features to high-level semantic space. $\mathbf{F}_{aggregated}$ is input aggregated visual feature vector, $\mathcal{R}_{residual}$ represents residual connection function, maintaining integrity of original feature information through skip connections, ensuring low-level visual details can directly influence final semantic representation generation process.

Gated fusion achieves dynamic integration:

$$\mathbf{S}_{refined} = \mathbf{g} \odot \mathbf{S}_{visual} + (1 - \mathbf{g}) \odot \mathbf{S}_{text} \quad (9)$$

Where gating weights are:

$$\mathbf{g} = \sigma(\mathbf{W}_{gate}[\mathbf{S}_{visual}; \mathbf{S}_{text}] + \mathbf{b}_{gate}) \quad (10)$$

In the gated fusion mechanism, $\mathbf{S}_{refined}$ represents final refined semantic representation, \mathbf{g} is adaptive gating weight vector controlling fusion ratio of visually-derived semantics and text semantics. \mathbf{S}_{visual} and \mathbf{S}_{text} respectively represent visually-derived semantic representation and original text semantic representation, \odot denotes element-wise multiplication operation. Gating weight \mathbf{g} is calculated through sigmoid activation function σ , \mathbf{W}_{gate} is weight matrix of gating network, \mathbf{b}_{gate} is bias vector, brackets denote concatenation operation of two semantic vectors. This mechanism can adaptively adjust fusion weights of different semantic information sources based on current feature quality and relevance, increasing weight of \mathbf{S}_{visual} when visual feature quality is high, otherwise relying more on text semantic information, achieving dynamically balanced semantic fusion strategy.

3.2.3 Interaction Quality Assessment and Convergence Control

The interaction quality assessment mechanism regulates bidirectional interaction through monitoring feature stability, quality metrics, and system anomalies. Convergence occurs when feature changes fall below thresholds, quality improves plateau, and no anomalies are detected, optimizing computational efficiency while maintaining representation quality.

4 Results

4.1 Experimental Setup and Implementation Details

This study utilized BraTS 2020 dataset comprising 369 multi-institutional MRI scans with four co-registered sequences uniformly adjusted to 128×128×128 resolution [1, 20]. Implementation employed NVIDIA A100 GPU with medical CLIP adapter initialized from pre-trained CLIP ViT-B/32 weights and 3D U-Net backbone. Training utilized AdamW optimizer (learning rate: 1e-5 to 5e-5) with OneCycleLR scheduling, weight decay (1e-4), dropout regularization (0.1-0.3), and augmentation strategies.

Segmentation performance was assessed using Dice coefficient (0-1 range) quantifying volumetric overlap and 95% Hausdorff distance (HD95, millimeters) measuring boundary localization accuracy [21, 22]. This dual-metric approach provides comprehensive quality assessment, with Dice evaluating regional consistency while HD95 addresses boundary delineation precision [23, 24].

4.2 Qualitative Results

Visual assessment was conducted on representative cases spanning different tumor sizes and morphological complexities. Figure 4 illustrates segmentation results using standardized color coding: whole tumor (red), tumor core (green), and enhancing tumor (blue).

The proposed framework demonstrates robust performance across varying tumor presentations. In standard cases (upper row), the method accurately delineates tumor boundaries with smooth contours and correct hierarchical relationships. For challenging cases with irregular morphology and ambiguous boundaries (lower row), the framework maintains structural integrity while preserving fine-grained details, particularly at the enhancing tumor periphery where intensity variations are subtle.

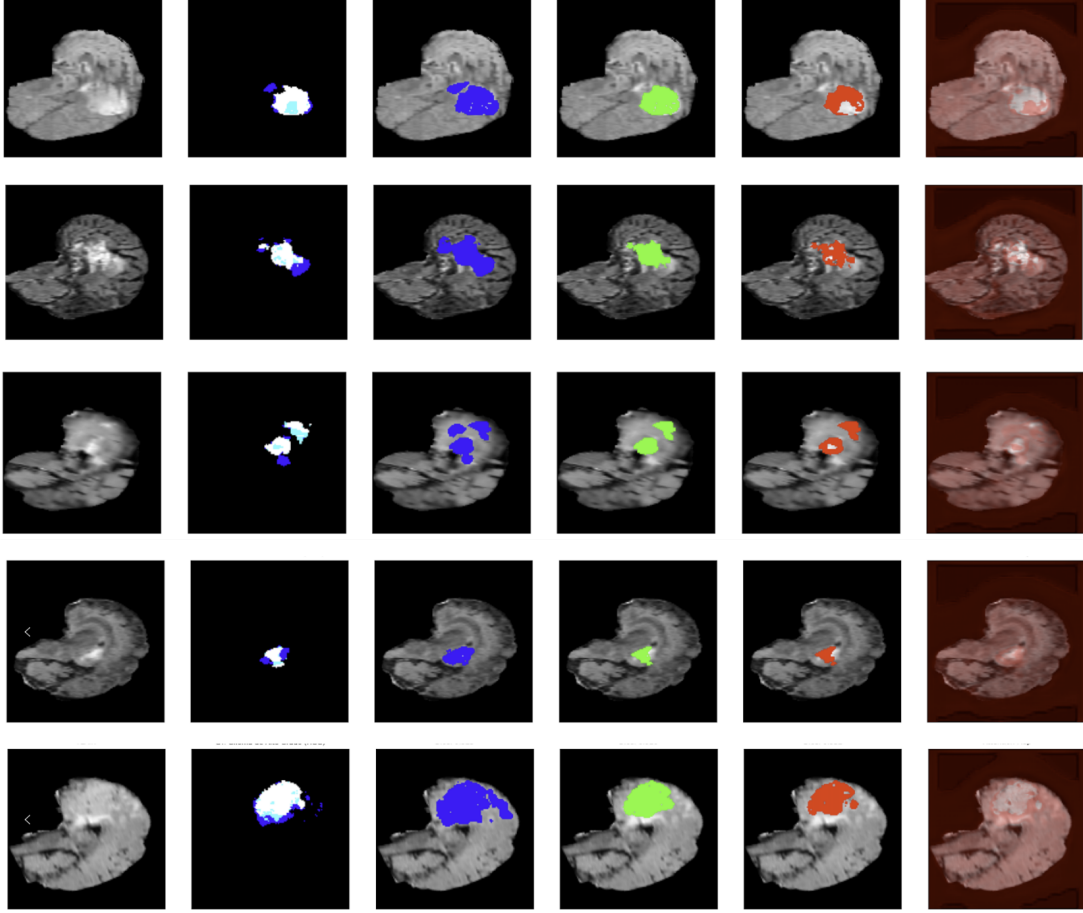


Figure 4: Qualitative evaluation visualization of brain tumor segmentation results. Color-coded overlay demonstrates segmentation effects for three key tumor sub-regions: whole tumor region (red), tumor core region (green), and enhancing tumor region (blue). (a) Upper row shows segmentation results for standard difficulty cases. (b) Lower row demonstrates recognition capability for complex pathological structures in highly challenging cases

4.3 Ablation Study

4.3.1 Component Contribution Analysis

To systematically evaluate the contribution of each architectural component, ablation experiments were conducted following established protocols in medical image analysis [25]. Three configurations were tested against the complete model: (1) removal of semantic processing branch to assess semantic information contribution, (2) disabling spatial constraint branch to evaluate anatomical prior importance, and (3) attempted visual processing branch removal to verify its fundamental role. All configurations maintained identical training protocols with 5-fold cross-validation to ensure statistical reliability [26].

The ablation results reveal distinct contributions of each component. Removing the semantic module resulted in a 0.66% decrease in average Dice coefficient ($0.8505 \rightarrow 0.8449$) but more notably a 23.6% degradation in HD95 distance ($2.8256\text{mm} \rightarrow 3.4913\text{mm}$), indicating semantic information critically enhances boundary precision. Spatial constraint removal showed minimal impact on Dice scores (0.51% decrease) but caused significant boundary accuracy degradation, particularly for tumor core (HD95: $2.8908\text{mm} \rightarrow 3.8763\text{mm}$). The visual module proved indispensable as its removal prevented model convergence entirely. These findings demonstrate that while all components contribute synergistically, semantic and spatial modules primarily enhance boundary delineation accuracy rather than volumetric overlap.

Table 1: Ablation study of component contributions to segmentation performance. The table shows Dice Similarity Coefficient and 95% Hausdorff Distance metrics for different model configurations across whole tumor (WT), tumor core (TC), and enhancing tumor (ET) regions

Configuration	Dice Similarity Coefficient				95% Hausdorff Distance (mm)			
	Mean	WT	TC	ET	Mean	WT	TC	ET
Full Model (Proposed)	0.8505	0.9022	0.8662	0.7830	2.8256	3.0736	2.8908	2.5124
w/o Semantic Module	0.8449	0.8871	0.8599	0.7876	3.4913	3.4370	3.4739	3.5631
w/o Spatial Constraints	0.8462	0.8931	0.8598	0.7858	3.4595	3.4264	3.8763	3.0758
w/o Visual Module	–	–	–	–	–	–	–	–

4.3.2 Semantic Integration Strategy Evaluation

To validate the effectiveness of the proposed multi-view CNN with attention pooling fusion strategy, comparative experiments were conducted against alternative semantic integration architectures. Recognizing that fusion strategy selection critically impacts multi-modal segmentation performance [27], we evaluated: (1) the proposed multi-view CNN with attention pooling for 3D medical image-text fusion, (2) CNN+Transformer architecture combining convolutional features with cross-modal Transformer fusion, and (3) multi-view CNN with standard attention replacing the pooling mechanism. These configurations represent current approaches in hybrid deep learning for medical image analysis [28, 29].

Table 2: Comparative evaluation of semantic fusion strategies for CLIP integration. Performance metrics include Dice Similarity Coefficient and 95% Hausdorff Distance (HD95) across three fusion approaches

Fusion Strategy	Dice Similarity Coefficient				95% Hausdorff Distance (mm)			
	Mean	WT	TC	ET	Mean	WT	TC	ET
Proposed Method	0.8505	0.9022	0.8662	0.7830	2.8256	3.0736	2.8908	2.5124
CNN + Transformer	0.8445	0.8990	0.8555	0.7790	4.2016	4.0895	4.4882	4.0270
Multi-view CNN + Attention	0.8485	0.8913	0.8666	0.7876	3.4323	3.4295	3.4960	3.3713

The proposed attention pooling strategy demonstrates superior performance across all metrics. Average Dice coefficient reaches 0.8505, exceeding CNN+Transformer (0.8445, 0.71% improvement) and multi-view CNN+attention (0.8485, 0.24% improvement). More significantly, boundary accuracy shows substantial improvements with HD95 of 2.8256mm, representing 32.8% and 17.7% reductions compared to alternatives. The CNN+Transformer approach exhibits degraded boundary precision across all tumor regions, potentially due to computational complexity when processing high-resolution 3D volumes. These results validate the effectiveness of attention pooling for adaptive multi-scale semantic feature aggregation in 3D medical image-text fusion tasks.

4.3.3 Bidirectional Interaction Mechanism Analysis

The effectiveness of the Bidirectional Interactive Visual-semantic Attention (BIVA) mechanism was evaluated through controlled experiments comparing bidirectional and unidirectional interaction modes. Three configurations were tested: (1) bidirectional interaction implementing complete information exchange between visual and semantic features, (2) semantic→visual mode retaining only semantic guidance while disabling reverse interaction, and (3) visual→semantic mode preserving visual refinement while removing semantic guidance. This experimental design isolates the specific contributions of each interaction direction.

Table 3: Evaluation of bidirectional versus unidirectional attention mechanisms. Comparison of information flow directions and their impact on segmentation performance metrics

Interaction Mode	Dice Similarity Coefficient				95% Hausdorff Distance (mm)			
	Mean	WT	TC	ET	Mean	WT	TC	ET
Bidirectional (Proposed)	0.8505	0.9022	0.8662	0.7830	2.8256	3.0736	2.8908	2.5124
Semantic→Visual Only	0.8476	0.9066	0.8593	0.7770	2.8836	2.2724	2.9277	3.4507
Visual→Semantic Only	0.8442	0.8892	0.8456	0.7977	3.7660	4.2158	4.3664	2.7158

Analysis reveals complementary strengths of each interaction direction. The semantic→visual configuration excels in whole tumor recognition (Dice: 0.9066, HD95: 2.2724mm), demonstrating effective semantic guidance for large-scale structures. However, enhancing tumor boundary accuracy deteriorates (HD95: 3.4507mm), indicating limitations in fine-grained detail preservation. Conversely, visual→semantic mode improves enhancing tumor overlap (Dice: 0.7977) but exhibits poor overall boundary accuracy (average HD95: 3.7660mm). The bidirectional approach achieves optimal balance across all metrics by leveraging mutual refinement, validating the hypothesis that iterative information exchange between modalities produces more robust segmentation than unidirectional guidance alone.

4.4 Comparison with State-of-the-Art Methods

To establish the performance positioning of the proposed framework, systematic comparison was conducted against contemporary state-of-the-art methods on the BraTS 2020 test set. Following standardized benchmarking protocols [30, 31], we evaluated three representative architectures: SCAU-Net (2023) implementing spatial-channel attention fusion mechanisms, CA-Net (2022) representing cross-attention network paradigms, and 3D U-Net (2021) establishing baseline performance for volumetric segmentation. All methods were evaluated under identical preprocessing pipelines and metrics to ensure fair comparison [32, 33].

Table 4: Quantitative comparison with existing brain tumor segmentation methods on BraTS 2020 test set. Methods are ordered by year of publication

Method	Dice Similarity Coefficient				95% Hausdorff Distance (mm)			
	Mean	WT	TC	ET	Mean	WT	TC	ET
Proposed Framework	0.8505	0.9022	0.8662	0.7830	2.8256	3.0736	2.8908	2.5124
SCAU-Net (2023)	0.8464	0.8995	0.8559	0.7837	2.9365	2.8423	2.9137	3.0534
CA-Net (2022)	0.7531	0.7861	0.7556	0.7175	9.1844	10.5143	9.8776	7.1613
3D U-Net (2021)	0.8346	0.8887	0.8099	0.7277	4.9785	3.7392	5.0812	5.7379

The proposed framework demonstrates consistent improvements across all evaluation metrics. Average Dice coefficient reaches 0.8505, surpassing SCAU-Net by 0.48%, CA-Net by 12.9%, and 3D U-Net by 1.9%. More pronounced improvements emerge in boundary delineation accuracy, with average HD95 of 2.8256mm representing reductions of 3.6%, 69.2%, and 43.2% respectively. Notably, the framework achieves superior performance on the challenging enhancing tumor segmentation task (Dice: 0.7830, HD95: 2.5124mm), where accurate delineation is critical for treatment planning. The substantial improvement over CA-Net suggests that multi-modal semantic integration provides advantages beyond purely attention-based approaches, while marginal gains over SCAU-Net validate the effectiveness of bidirectional interaction mechanisms in refining state-of-the-art architectures.

5 Conclusion

This study establishes multi-modal fusion and bidirectional interaction as foundational paradigms through two innovations: Multi-modal Semantic Fusion Adapter integrating spatial, semantic, and visual features; and Bidirectional Interactive Visual-semantic Attention implementing dynamic iterative refinement. Validation on BraTS 2020 dataset demonstrates superior performance with average Dice of 0.8505 and HD95 of 2.8256mm.

The framework extends beyond brain tumor segmentation, providing methodologies including medical CLIP adaptation, hierarchical semantic decoupling, and bidirectional attention applicable across medical imaging domains. Future research encompasses multi-scale analysis, integration of genomic modalities, and application-specific variants [34]. The architecture supports emerging applications in personalized medicine, digital trials, and virtual health assistants [35], establishing standards for multi-modal medical image analysis.

Acknowledgments

We acknowledge the BraTS challenge organizers for providing the standardized dataset utilized in this investigation. We thank the anonymous reviewers for their constructive comments that helped improve this manuscript.

References

- [1] Menze, B. H., Jakab, A., Bauer, S. et al.: The Multimodal Brain Tumor Image Segmentation Benchmark (BRATS). *IEEE Trans Med Imaging* 34(10), 1993-2024 (2015). <https://doi.org/10.1109/TMI.2014.2377694>
- [2] Liu, Z., Tong, L., Chen, L. et al.: Deep learning based brain tumor segmentation: a survey. *Complex Intell Syst* 9, 1001-1026 (2023). <https://doi.org/10.1007/s40747-022-00815-5>
- [3] Hatamizadeh, A., Nath, V., Tang, Y. et al.: Swin UNETR: Swin Transformers for Semantic Segmentation of Brain Tumors in MRI Images. In: *Brainlesion: Glioma, Multiple Sclerosis, Stroke and Traumatic Brain Injuries*, pp. 272-284. Springer (2022). https://doi.org/10.1007/978-3-031-08999-2_22
- [4] Zhou, H. Y., Guo, J., Zhang, Y. et al.: nnFormer: Volumetric Medical Image Segmentation via a 3D Transformer. *IEEE Trans Image Process* 32, 4036-4045 (2023). <https://doi.org/10.1109/TIP.2023.3293771>
- [5] Hatamizadeh, A., Tang, Y., Nath, V. et al.: UNETR: Transformers for 3D Medical Image Segmentation. In: *Proceedings of the IEEE/CVF Winter Conference on Applications of Computer Vision (WACV)*, pp. 574-584 (2022). <https://doi.org/10.1109/WACV51458.2022.00181>
- [6] Isensee, F., Jaeger, P. F., Kohl, S. A. A. et al.: nnU-Net for Brain Tumor Segmentation. In: *Brainlesion: Glioma, Multiple Sclerosis, Stroke and Traumatic Brain Injuries*, pp. 118-132. Springer (2021). https://doi.org/10.1007/978-3-030-72087-2_11
- [7] Zhang, S., Xu, Y., Usuyama, N. et al.: BiomedCLIP: a multimodal biomedical foundation model pretrained from fifteen million scientific image-text pairs. *arXiv preprint arXiv:2303.00915* (2023)
- [8] Zhao, Z., Gu, Y., Xu, Y. et al.: CLIP in Medical Imaging: A Comprehensive Survey. *Med Image Anal* 99, 103551 (2025). <https://doi.org/10.1016/j.media.2025.103551>
- [9] Guo, Y., Wang, X., Chen, Y. et al.: Multimodal MRI Image Decision Fusion-Based Network for Glioma Classification. *Front Oncol* 12, 819673 (2022). <https://doi.org/10.3389/fonc.2022.819673>
- [10] Li, K., Li, Y., Wang, Z. et al.: MSFR-Net: Multi-Modality and Single-Modality Features Reunion Network for Brain Tumor Segmentation. *Med Phys* 50(10), 6342-6356 (2023). <https://doi.org/10.1002/mp.15933>
- [11] Zhang, Q., Xiao, L., Li, W. et al.: Medical image fusion with deep neural networks. *Sci Rep* 14, 8665 (2024). <https://doi.org/10.1038/s41598-024-58665-9>
- [12] You, S., Lei, Y., Wang, S. et al.: CXR-CLIP: Toward Large Scale Chest X-ray Language-Image Pre-training. In: *Medical Image Computing and Computer Assisted Intervention – MICCAI 2023*, pp. 101-111. Springer (2023). https://doi.org/10.1007/978-3-031-43895-0_10
- [13] Wang, X., Li, Z., Chen, Y. et al.: CTBANet: Convolution transformers and bidirectional attention for medical image segmentation. *Alexandria Eng J* 91, 200-210 (2024). <https://doi.org/10.1016/j.aej.2024.01.020>
- [14] Irene, K., Christian, F., Sophia, B. et al.: Vision-language models for medical report generation and visual question answering: a review. *Front Artif Intell* 7, 1430984 (2024). <https://doi.org/10.3389/frai.2024.1430984>
- [15] Wang, L., Zhang, Y., Chen, Z. et al.: Anatomical Prior-Based Automatic Segmentation for Cardiac Substructures from Computed Tomography Images. *Bioengineering* 10(11), 1267 (2023). <https://doi.org/10.3390/bioengineering10111267>
- [16] Zhou, T., Li, L., Bredell, G. et al.: Quality-aware memory network for interactive volumetric image segmentation. In: *Medical Image Computing and Computer Assisted Intervention – MICCAI 2021*, pp. 560-570. Springer (2021). https://doi.org/10.1007/978-3-030-87196-3_52
- [17] Li, Y., Wang, N., Shi, J. et al.: Transformers in medical imaging: A survey. *Med Image Anal* 88, 102802 (2023). <https://doi.org/10.1016/j.media.2023.102802>
- [18] He, K., Chen, X., Xie, S. et al.: Recent progress in transformer-based medical image analysis. *Comput Biol Med* 164, 107268 (2023). <https://doi.org/10.1016/j.combiomed.2023.107268>
- [19] Wasserthal, J., Breit, H. C., Meyer, M. T. et al.: TotalSegmentator: Robust Segmentation of 104 Anatomic Structures in CT Images. *Radiology Artif Intell* 5(5), e230024 (2023). <https://doi.org/10.1148/ryai.230024>
- [20] Baid, U., Ghodasara, S., Mohan, S. et al.: The RSNA-ASNR-MICCAI BraTS 2021 Benchmark on Brain Tumor Segmentation and Radiogenomic Classification. *arXiv preprint arXiv:2107.02314* (2021). <https://doi.org/10.48550/arXiv.2107.02314>
- [21] Yeghiazaryan, V., Voiculescu, I.: Family of boundary overlap metrics for the evaluation of medical image segmentation. *J Med Imaging* 5(1), 015006 (2018). <https://doi.org/10.1117/1.JMI.5.1.015006>

- [22] Jungo, A., Meier, R., Ermis, E. et al.: On the effect of inter-observer variability for a reliable estimation of uncertainty of medical image segmentation. In: Medical Image Computing and Computer Assisted Intervention – MICCAI 2018, pp. 682-690. Springer (2018). https://doi.org/10.1007/978-3-030-00928-1_77
- [23] Taha, A. A., Hanbury, A.: Metrics for evaluating 3D medical image segmentation: analysis, selection, and tool. BMC Med Imaging 15, 29 (2015). <https://doi.org/10.1186/s12880-015-0068-x>
- [24] Kainmueller, D., Lamecker, H., Seim, H. et al.: Towards a guideline for evaluation metrics in medical image segmentation. BMC Res Notes 15, 210 (2022). <https://doi.org/10.1186/s13104-022-06096-y>
- [25] Müller, D., Soto-Rey, I., Kramer, F.: Towards a guideline for evaluation metrics in medical image segmentation. BMC Res Notes 15, 210 (2022). <https://doi.org/10.1186/s13104-022-06096-y>
- [26] Varoquaux, G., Raamana, P. R., Engemann, D. A. et al.: A Guide to Cross-Validation for Artificial Intelligence in Medical Imaging. Radiology 308(2), e230785 (2023). <https://doi.org/10.1148/radiol.230785>
- [27] Wang, S., Zhou, M., Liu, Z. et al.: Medical image segmentation using deep learning: A survey. IET Image Process 16(5), 1243-1267 (2022). <https://doi.org/10.1049/ipr2.12419>
- [28] Fu, S., Lu, Y., Wang, Y. et al.: A Review of Deep-Learning-Based Medical Image Segmentation Methods. Sustainability 13(3), 1224 (2021). <https://doi.org/10.3390/su13031224>
- [29] Heimann, T., Meinzer, H. P.: Statistical shape models for 3D medical image segmentation: A review. Med Image Anal 13(4), 543-563 (2009). <https://doi.org/10.1016/j.media.2009.05.004>
- [30] Litjens, G., Kooi, T., Bejnordi, B. E. et al.: A survey on deep learning in medical image analysis. Med Image Anal 42, 60-88 (2017). <https://doi.org/10.1016/j.media.2017.07.005>
- [31] Sayed, M., Alsharef, M., Sayed, F. et al.: Advances in Medical Image Segmentation: A Comprehensive Review of Traditional, Deep Learning and Hybrid Approaches. Bioengineering 11(10), 1034 (2024). <https://doi.org/10.3390/bioengineering11101034>
- [32] Zhang, Y., Liu, H., Hu, Q.: A 3D medical image segmentation network based on gated attention blocks and dual-scale cross-attention mechanism. Sci Rep 15, 2024 (2025). <https://doi.org/10.1038/s41598-025-90339-y>
- [33] Alqudah, A. M., Qazan, S., Masad, I. S.: Medical image analysis using deep learning algorithms. Front Public Health 11, 1273666 (2023). <https://doi.org/10.3389/fpubh.2023.1273666>
- [34] Sun, K., Xue, S., Zhang, P. et al.: Medical Multimodal Foundation Models in Clinical Diagnosis and Treatment: Applications, Challenges, and Future Directions. arXiv preprint arXiv:2412.02621 (2024). <https://doi.org/10.48550/arXiv.2412.02621>
- [35] Acosta, J. N., Falcone, G. J., Rajpurkar, P. et al.: Multimodal biomedical AI. Nat Med 28(9), 1773-1784 (2022). <https://doi.org/10.1038/s41591-022-01981-2>